López-Andarias J, Mejías SH, Sakurai T, et al. Toward Bioelectronic Nanomaterials: Photoconductivity in Protein-Porphyrin Hybrids Wrapped around SWCNT. Advanced Functional Materials. 2017:1704031. doi: 10.1002/adfm.201704031.

DOI: 10.1002/ ((please add manuscript number))

Article type: Toward bioelectronic nanomaterials: photoconductivity in protein-porphyrin hybrids wrapped around SWCNT

Dr. Javier López-Andarias,‡[a] Dr. Sara H. Mejías,‡[b] Dr. Tsuneaki Sakurai,[c] Wakana Matsuda,[c] Prof. Shu Seki,[c] Dr. Ferran Feixas,[d] Dr. Sílvia Osuna,[d] Dr. Carmen Atienza,[a] Prof. Nazario Martín*[a],[b] and Dr. Aitziber L. Cortajarena*[b],[e],[f]*

((Optional Dedication))

Dr. J. López-Andarias, Dr. C. Atienza, Prof. N. Martín
[a] Departamento de Química Orgánica I, Facultad de Química, Universidad Complutense, E-28040 Madrid, Spain.
E-mail: nazmar@ucm.es, alcortajarena@cicbiomagune.es, cmatienz@ucm.es
Dr. S. H. Mejías, Dra. A. L. Cortajarena
[b] IMDEA-Nanociencia, C/ Faraday, 9, Campus de Cantoblanco, E-28049 Madrid, Spain
[e] CIC biomaGUNE, Paseo de Miramón 182, E-20009 Donostia-San Sebastian, Spain.
[f] Ikerbasque, Basque Foundation for Science, Mª Díaz de Haro 3, E-48013 Bilbao, Spain
Dr. F. Feixas, Dr. S. Osuna
[d] Institut de Química Computacional i Catàlisi and Departament de Química, Universitat de Girona, c/ Maria Aurèlia Capmany, 6, 17003 Girona, Spain
Dr. T. Sakurai, Dr. W. Matsuda, Prof. S. Seki
[c] Department of Molecular Engineering, Graduate School of Engineering, Kyoto University.

Keywords: Porphyrin, designed proteins, consensus tetratricopeptide repeat (CTPR), biomolecular templating, SWCNT, photoconductive materials

The development of sophisticated ordered functional materials is one of the important challenges in current science. One of the keys to enhance the properties of these materials is the control of the organization and morphology at different scales. In this work, we present a novel bioinspired methodology to achieve highly ordered donor/acceptor bionanohybrids using a designed repeat protein as scaffold, endowed with photoactive and electron donating porphyrin (P) units, to efficiently wrap around electron accepting SWCNT. A systematic experimental and theoretical study to evaluate the effect of the length of the protein reveals that longer proteins wrap around the SWCNT in a more efficient manner due to the stronger supramolecular interaction existing between the inner concave surface of the protein (namely Trp and His residues) and the convex surface of the (7,6)-SWCNT. Interestingly, spectroscopy and X-ray diffraction data further confirm that the so-called protein-P-SWCNT donor-acceptor bio-nanohybrids retain the original protein structure. Finally, the new bio-nanohybrids show a remarkable enhancement on the photoconductivity values (FP-TRMC technique) demonstrating that the major charge carriers of electrons are injected into the SWCNTs and move along the 1D-structures.

1. Introduction

Symbiosis between carbon nanotubes (CNTs) and biological entities to create nanohybrid materials is a cutting-edge area with high impact in fields such as bio-medicine, sensing and energy production, just to name a few.[1] Up to now, DNA-CNT bionano hybrids are leading this research area due to the well-established and accurate design and manufacture of artificial nucleic-acid structures.[2] In contrast, the use of proteins for the generation of protein-CNT hybrids for optoelectronic applications is not so expanded presumably in behalf of the gap between the development of protein design comparing with that of DNA nanotechnology. However, in the last years, both computational and experimental studies have demonstrated the great potential of proteins and oligopeptides as biological frameworks for the functionalization and organization of CNTs. The main reason that makes proteins a powerful tool for nanotechnological applications is the extended number of building blocks comparing with DNA, with 20 different proteinogenic amino acids considering only the canonical ones, with the concomitant possibility to tune more precisely the final properties of the so-called biological materials.[3]

Rationally, a requirement of these biological nanohybrids for being applied in light-harvesting and electron transfer devices is the introduction of an appropriate electron donor entity, acting the CNT as the electron acceptor material. In this line, a singular example presented by D’Souza and co-workers can be found in literature in which a three-component hybrid, porphyrin-DNA-CNT, is utilized for photoinduced electron transfer processes.[4] However, to the best of our knowledge, donor-protein-CNT hybrids remain still unexplored.

In a previous work, we presented a novel bioinspired approach in which photoactive porphyrin derivatives were covalently connected to the helical scaffold of a designed repeat protein, in particular a consensus tetratricopeptide repeat (CTPR) protein, giving rise to an ordered and oriented bio-organic conjugate.[5] Specifically, a mutated CTPR protein with four repeated units was designed, introducing two cysteine residues in each repeat to provide unique reactivity for the immobilization of the porphyrin derivatives. The hybrid conjugates retained the structure and assembly properties of the protein scaffold and displayed the spectroscopic features of orderly aggregated porphyrins along the protein structure.[5] Herein, we present the creation of novel protein-SWCNT donor-acceptor bio-nanohybrids from our recent bioinspired approach with potential applications in the *so-called* “biomolecular electronics”.

2. Results and Dicussion

2.1. **Compatibility of morphology and composition of CTPR proteins and SWCNTs**

The TPR motif consists of 2-20 tandem-repeats of 34 amino acids residues adopting a helix-turn-helix arrangement.[6] Because of their modular nature repeat proteins are well suited to be used as biomolecular scaffolds.[7] These CTPR repeats generate a right-handed superhelical structure[8] producing two protein surfaces: an inner concave face which contributes mainly to ligand recognition in natural domains and a solvent exposed outer convex face.[8b] Thus, the concave face presents an attractive frame for the accommodation of the hydrophobic SWCNT surface (Figure 1a).

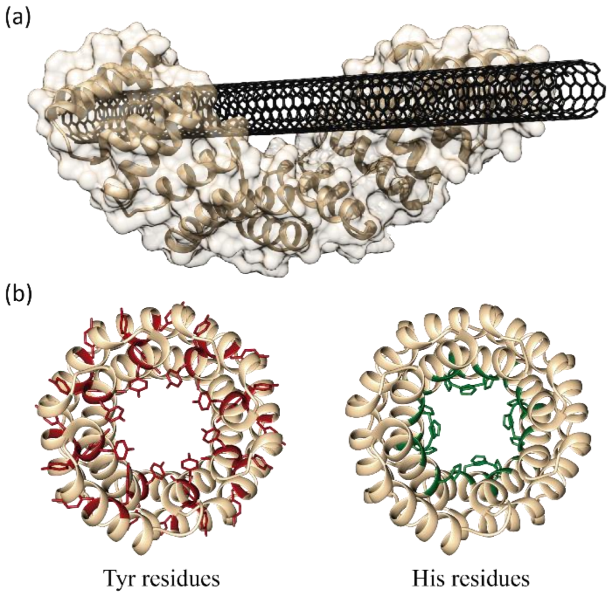

Figure 1. Suitability of morphology and composition of CTPR proteins with SWCNTs. (a) Model of a CTPR8 (PDB ID: 2AVP[8b]) and a (7,6)-SWCNT showing the morphological compatibility between the concave face of the protein and the SWCNT surface. (b) Axial view along the superhelical axis of a CTPR8 highlighting the Tyr residues (red) and the engineered His residues (green).

Favorable binding between protein residues and CNT surface is mandatory for an effective interaction. In this sense, a deep search in literature of the reported non-covalent forces ruling the adsorption of peptides and proteins onto CNT surfaces was made. This examination was aimed to validate the composition of the protein and, if possible, to modify those non-conserved positions of the repeat sequence by more interacting amino acids, without affecting the structure of the protein framework.

As described in recent theoretical and experimental works, the strongest interacting residues with CNTs are those bearing aromatic units in their side chains by establishing π-π and XH$\cdots\pi$ (X = C, N) contacts.[3e, 9] In this sense, Trp, Tyr, Phe and His are good candidates to be localized in those positions forming part of the concave face in CTPR proteins. Among these, important experimental evidences demonstrated that peptide sequences rich in Trp and His show strong interactions with the CNT surface.[3f, 10]

As previously described, surface exposed residues on the concave face in TPR proteins are mainly localized in helix A (Figure 2a), and usually encode specific binding to target guests.[11] Considering this fact, and the understanding of the consensus positions in TPR sequence, positions 5 and 9, both localized on the concave protein surface, were modified by His residues to increase the interaction with the CNT wall. Luckily, Tyr residues are found in the original sequence of CTPR unit, two of them with the phenol group pointing through the concave face. Altogether, two His and two Tyr in each repeat fragment could play a major role in the favorable interaction of the protein with the CNT (Figure 1b).

2.2. **Design and synthesis of CTPR proteins and conjugates.**

For the study described herein, we employ three mutated TPR proteins with different number of CTPR repeats (CTPR4, CTPR8 and CTPR16) and their corresponding conjugates (CTPR4-P, CTPR8-P and CTPR16-P) with our previously described zinc-metalloporphyrin P, bearing ethyleneglycol chains to ensure water solubility and a cysteine-reactive maleimide group for the conjugation with the protein (See SI for further description of P). The previously described mutated CTPR4 was used as the smallest protein scaffold, with a dimension of approximately 40 x 36 Å and eight cysteine residues in the outer area of the superhelix, in particular, in the four loops of the protein, for the conjugation with the maleimide-type porphyrin P. The distance between the Cys side chains is between 7 to 8 Å, in the order of the distance required to establish π-π interactions between the porphyrin rings. Meanwhile, two new mutated proteins were designed, that is, CTPR8 and CTPR16. CTPR8 consisted on eight repeat units comprising one superhelical turn with overall molecular dimensions of approximately 80 x 36 Å and 16 cysteine residues. Finally, CTPR16, with two superhelical turns, a dimension of 160 x 36 Å and 32 cysteine residues, was the largest biological framework. Moreover, two His residues per repeat unit were introduced in the sequence of the proteins (Figure 2a). As expected, the two Cys and two His mutations in each repeat unit did not significantly affect the helical structure of the protein scaffold. Thus, well-expressed, stable protein samples with the same α-helical structure as the parent protein were obtained (Figure 2b,c).

The designed proteins and metalloporphyrin P were conjugated using the maleimide-cysteine chemistry and the analysis of the samples by gel electrophoresis showed that conjugates of higher molecular weight than their corresponding CTPR proteins were obtained. Specifically, conjugates presented more than double weight comparing with their unfunctionalized proteins, meaning a near quantitative yield in the conjugation reaction of the cysteine residues. When the gel was imaged without staining, the porphyrin fluorescence signal could be detected only in the lanes containing conjugates holding the porphyrin moieties, as expected (Figure S1).

The purification of the protein-porphyrin conjugates from the excess of free porphyrin is a mandatory step to produce homogenous hybrid structures. It was successfully carried out using size exclusion chromatography with the same conditions previously reported for the purification of the CTPR4-porphyrin conjugates.[5] As predicted, the elution time decreased while increasing the size of the conjugate (Figure S1).

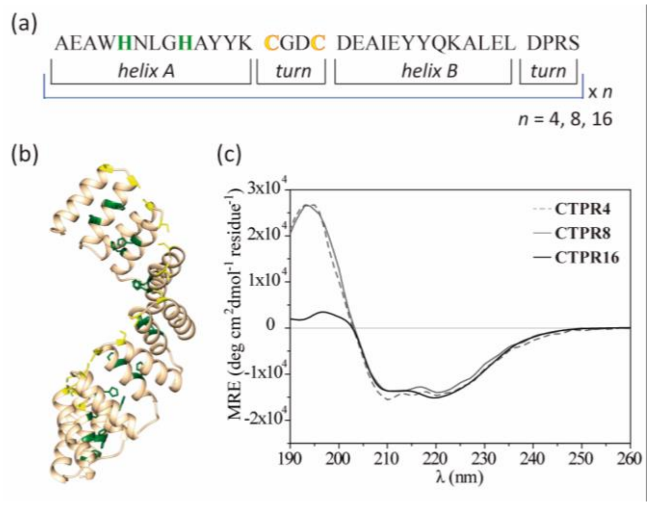

Figure 2. Design and synthesis of mutated CTPR proteins. (a) Sequence of amino acids of the repeat CTPR module, highlighting the positions 5 and 9 mutated to Histidine (green) and 14 and 17 mutated to Cysteine (yellow). (b) Ribbon representation of the mutated CTPR8 with

Histidine residues in green and Cysteine residues in yellow. (c) CD spectra of mutated CTPR4, CTPR8 and CTPR16.

A precise quantification of the number of porphyrins attached to each protein was not possible to elucidate by mass spectrometry due to the high content in porphyrin molecules and the high molecular weight of these conjugates (80-87 kDa for CTPR8-P with 14-16 porphyrins and 158-171 kDa for CTPR16-P with 28-32 porphyrins), which probably difficult the volatilization of the samples. The effectiveness of the conjugation reaction was qualitatively demonstrated using absorption spectroscopy by the relative intensity of the Soret absorption band of porphyrin P, at 430 nm, compared to the protein absorption band, at 280 nm. Figure 3a shows, on one hand, that the Soret and the Q-bands in the CTPR8-P and CTPR16-P conjugates were not displaced to neither higher or lower wavelengths comparing to the previously reported UV-*vis* spectrum of CTPR4-P, thus, the location of the porphyrins and their electronic communication should be comparable, that is, establishing *J*-type aggregates. On the other hand, the ratio of the absorbance at λ = 430 nm respecting to λ = 280 nm in the three conjugates unambiguously proved that the relative amount of porphyrins is maintained while the dimension of the protein is enlarged. In our previous work, we demonstrated by mass spectrometry that 6 to 8 porphyrins on average were attached to the CTPR4. Therefore, we can conclude that the effectiveness of the conjugation reaction is maintained in all the cases and is unaffected by the size increment in CTPR8 – 12 to 16 porphyrins – and CTPR16 –24 to 32 porphyrins (Figure 3b).

Regarding secondary structure of the protein scaffold within the conjugate and the spatial organization of the porphyrin moieties, CD studies were carried out. In the absorption region of proteins, that is, from 260 to 190 nm, all conjugates revealed the feature CD signal for α-helical secondary structure presented in CTPR proteins (Figures 3c and S2). Furthermore, optical activity is exhibited in the Soret absorption band of achiral porphyrins, indicating a chiral arrangement of these chromophores within the conjugates (Figure 3d and S2). These results confirmed the ability of all the mutated CTPR proteins employed in this work to act as robust biological scaffolds for ordering organic chromophores.

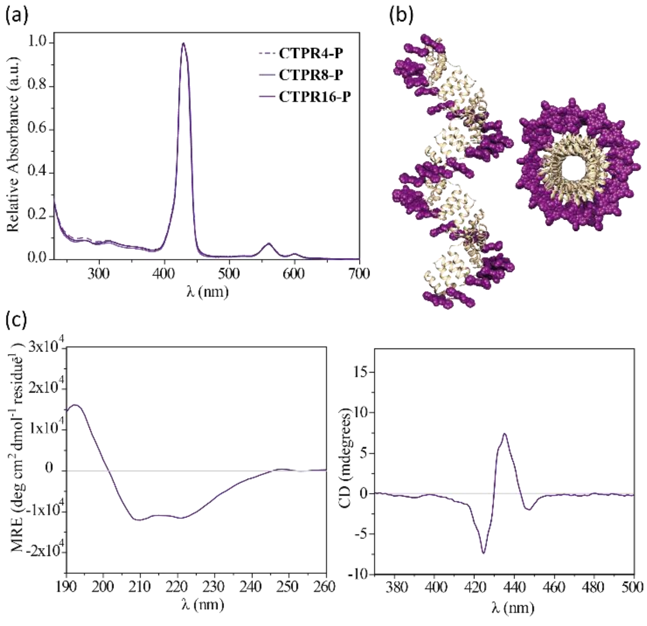

Figure 3. Spectroscopic characterization of bio-organic conjugates. (a) Normalized UV-*vis* spectra of conjugates CTPR4-P, CTPR8-P and CTPR16-P. (b) Representation of CTPR16-P from different views. (c) CD spectra of CTPR16-P in the protein absorption region. (d) CD spectra of CTPR16-P in the Soret band absorption region of the zinc-metalloporphyrin.

2.3. **Wrapping SWCNT by CTPR proteins and conjugates.**

After obtaining and characterizing the corresponding CTPR proteins and protein-porphyrin conjugates, they were evaluated as wrapping agents for SWCNTs. Both of them formed water-soluble hybrid assemblies with SWNTs, producing aqueous solutions that were stable for months in the fridge (Figure S3. See SI for complete description of the preparation of the nanohybrids).

Insights into protein-SWCNT and conjugate-SWCNT ground-state electronic interactions came from UV-*vis* spectroscopic experiments. The study performed on the protein-SWCNT nanohybrids is depicted in Figure 4a. Although only three lengths of CTPR proteins have been used for this study, some trends can be pointed out: at the same amount of protein, that is 0.005% (w/v), the larger systems were able to dissolve more effectively SWCNTs in aqueous media. In particular, CTPR16, with two completed superhelical turns, was the most efficient wrapping agent followed by CTPR8, with one superhelical turn. CTPR4, being the shortest biological scaffold, was also the least effective. All-atom Molecular Dynamics (MD) simulations of the CTPR4-16 in the presence of a 20 nm long (7,6) SWCNT were performed to rationalize their different binding capacity, and provide an atomistic description of the recognition process (Figure 5). For each system, three replicas of 100 ns unbiased MD simulations were initially run followed by 100 ns of accelerated Molecular Dynamics (aMD) to enhance conformational sampling (see SI for complete computational details). In the 200 ns (a)MD simulations, all CTPR4-16 systems gradually adopt a more extended conformation over the SWCNT surface, as observed in Figure 5 and in the increase of the standard deviation of the radius of gyration. The latter ranges from *ca.* 18.2 ±1.7, 29.0 ±2.1, and 47.9 ±3.0 Å for CTPR4-16, respectively. The more extended CTPR4-16 conformations maximize the π-π interactions of His, Tyr and Trp residues located in the concave face of the protein with the SWCNT. The access to these extended conformations is in agreement with the previously reported flexibility of the CTPR superhelices.[12] CTPR16 and CTPR8 systems can completely wrap the SWCNT. CTPR4 is less effective due to its shorter length that only covers half of the SWCNT perimeter. This is reflected in the binding affinities: CTPR16 exhibits by far the most favorable binding (-638.8 ±15.5 kcal/mol), followed by CTPR8 (-334.7 ±40.6 kcal/mol), and CTPR4 (-288.4 ±18.5 kcal/mol). Along the course of the simulations more favorable binding energies are obtained as the elongation of the protein chain enhances their interaction with the SWCNT (Figure 5).

The same comparative study was performed on the respective three conjugates. In order to establish the influence on the exfoliation and supramolecular functionalization of SWCNTs with the zinc metalloporphyrin fragment P in the conjugates, a control experiment was carried out using the non-conjugated porphyrin P (See SI for complete description). Figure S4 shows the result, remarking the slight presence of SWCNTs in solution and more than 90% of porphyrin P precipitated out, probably because of π-π interaction with the surface of nanotube, establishing porphyrin-SWCNT nanohybrids with no stability in water.

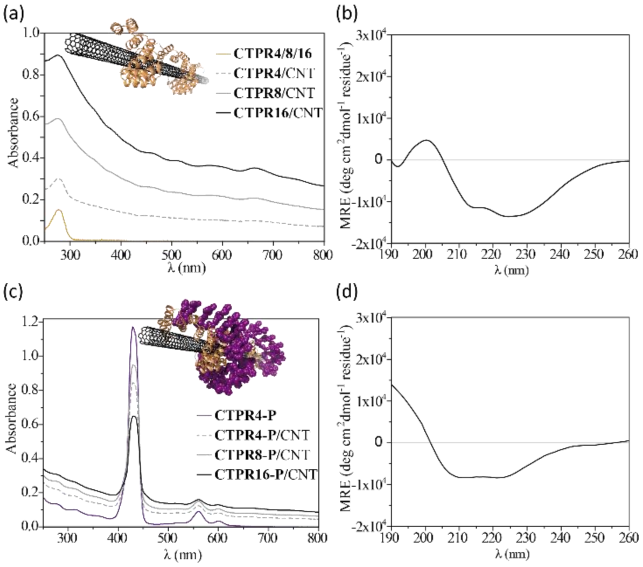

Figure 4. Spectroscopic characterization of the bio- and the bio-organic nanohybrids. (a) UV-*vis* spectra of CTPR4 (yellow line), CTPR4/CNT (grey dashed line), CTPR8/CNT (grey solid line) and CTPR16/CNT (black solid line). (b) CD spectrum of CTPR16/CNT. (c) UV-*vis* spectra of CTPR4-P (purple line), CTPR4-P/CNT (grey dashed line), CTPR8-P/CNT (grey solid line) and CTPR16-P/CNT (black solid line). (d) CD spectrum of CTPR16-P/CNT.

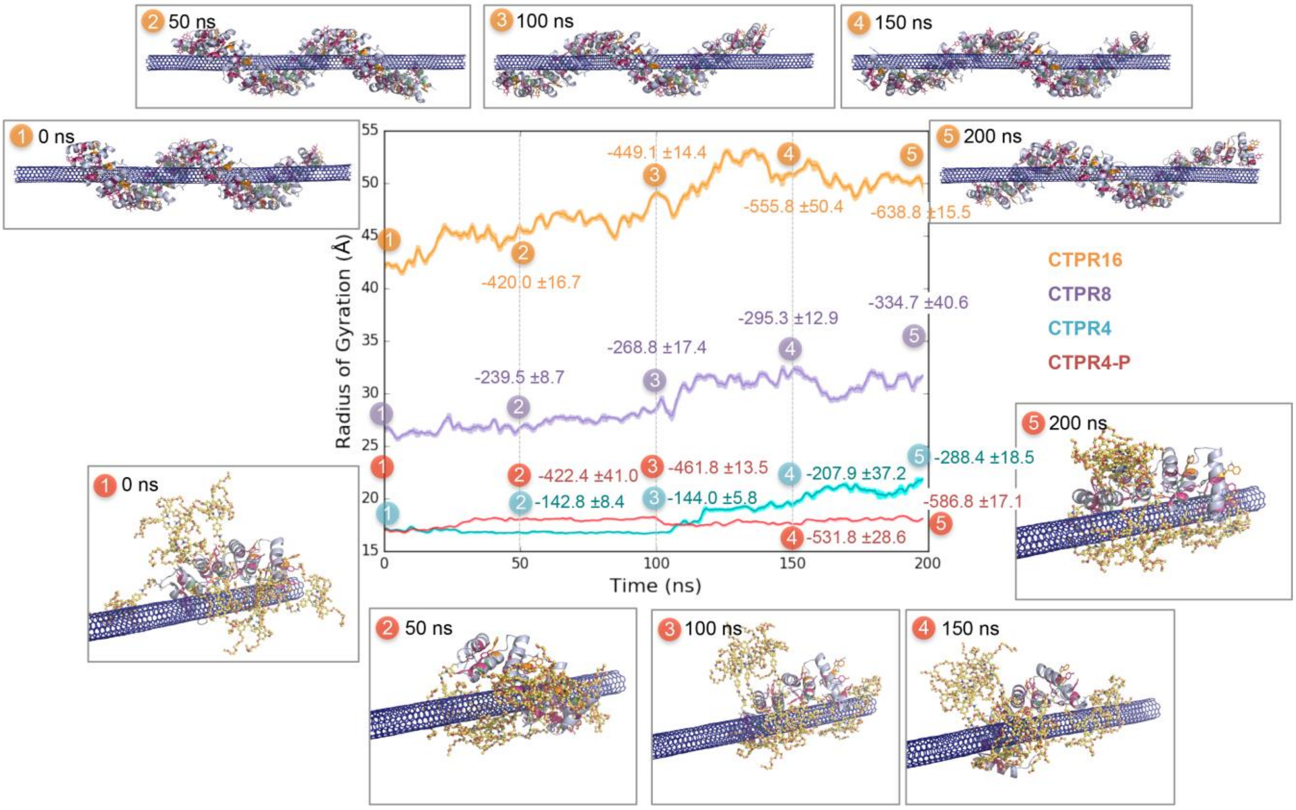

Figure 5. Representation of the evolution of the radius of gyration (in Å) of CTPR16 (in orange), CTPR8 (violet), CTPR4 (cyan), and the porphyrin conjugate CTPR4-P (red) along the 200 ns (a) MD simulations. The computed binding energies (in kcal/mol) are represented every 50 ns of simulation for all systems. In the case of CTPR16 and CTPR4-P some representative snapshots are also displayed.

UV-*vis* studies performed on the conjugates with SWCNTs are illustrated in Figure 4c with comparable results relating to their analogue non-conjugated proteins. The trend was similar to that in the proteins, that is, at the same amount of the conjugates, longer scaffolds were more effective wrapping agents for the carbon nanostructures. To rationalize the effect of porphyrin moieties on the binding affinities of the protein scaffolds with the SWCNT, MD simulations were performed on the smallest CTPR4-P/SWCNT conjugate (see Figure 5, and SI for computational details). The binding energies are substantially enhanced by the inclusion of porphyrins (-288.4 ±18.5 and -586.8 ±17.1 kcal/mol for CTPR4 and CTPR4-P, respectively). As shown in Figure 5, the increase in the binding affinity mainly comes from the interaction of the porphyrin moieties with the surface of the SWCNT, which completely wrap the nanotube perimeter by the end of the MD simulation. These results are in concordance with the effect observed in the visible range of the Soret band of the zinc-metalloporphyrins that decreased, in spite of the increasing intensities in the whole spectral region of protein-SWCNT (Figure 4c).

Structural integrity of the proteins and conjugates, when they are constituting their corresponding nanohybrids with SWCNTs, was proven by CD assays. Figure 4b,d and S5 show how the α-helix signature of CTPR framework is maintained in all the cases. The only difference to point out is the slight reduction in the dichroic signal comparing with the pristine samples without SWCNTs. This experimental finding could be attributed to a decrease of the protein/conjugate concentration during the centrifugation process. CNTs without a dense covering of proteinaceous material could precipitate out of the aqueous solution, carrying with them some wrapped macromolecules. Nevertheless, partial unfolding of the α-helices could be another explanation to take into account.

Once identified CTPR16 protein and its corresponding CTPR16-P conjugate as the best dissolving agents of SWCNTs, the following assays are described only for their resultant nanohybrids: concomitant studies came from Raman spectroscopy which provided valuable information regarding the interaction between both entities. The first evidence to note is that D band intensity, relating to G bands, reveals no difference comparing with pristine SWCNTs, as expected from a non-covalent interaction (Figure 6a). In contrast, G-modes, shown in Figure 6b, reveal a downshifted from 1592 cm^{-1} in pristine SWCNTs, to 1589 and 1585 cm^{-1} in CTPR16/CNT and CTPR16-P/CNT, respectively. Previous studies have demonstrated that the G band peak in CNTs shifts to lower frequencies when doping with electron donor agents and to higher frequencies with electron acceptor ones.[13] However, in a reported work using peptides as wrapping agents of SWCNTs, even with modified Phe residues by Tyr residues (more electron donor moieties), the G-mode is upshifted comparing with uncoated SWCNTs.

Only when comparing a Phe-rich peptide/CNT with a Tyr-rich peptide/CNT, a slight downshift of the G-mode was appreciated (0.6 cm^{-1}).[10a] However, in our current case, a remarkable downshift of 3 cm^{-1} in CTPR16/CNT comparing with pristine SWCNT was found (Figure 6b). This experimental finding attested the strong interactions of electron-donating residues in CTPR16 with the surface of the nanotube. In particular, the 32 His and 32 Tyr presented in the concave face of CTPR16 could be the responsible of such substantial shift to lower frequencies in the G band peak of SWCNTs. In the case of CTPR16-P conjugate, the effect was even more pronounced, with a downshift of 7 cm^{-1}, supplying evidence of a possible charge transfer process between the porphyrins and the SWCNTs (Figure 6b).

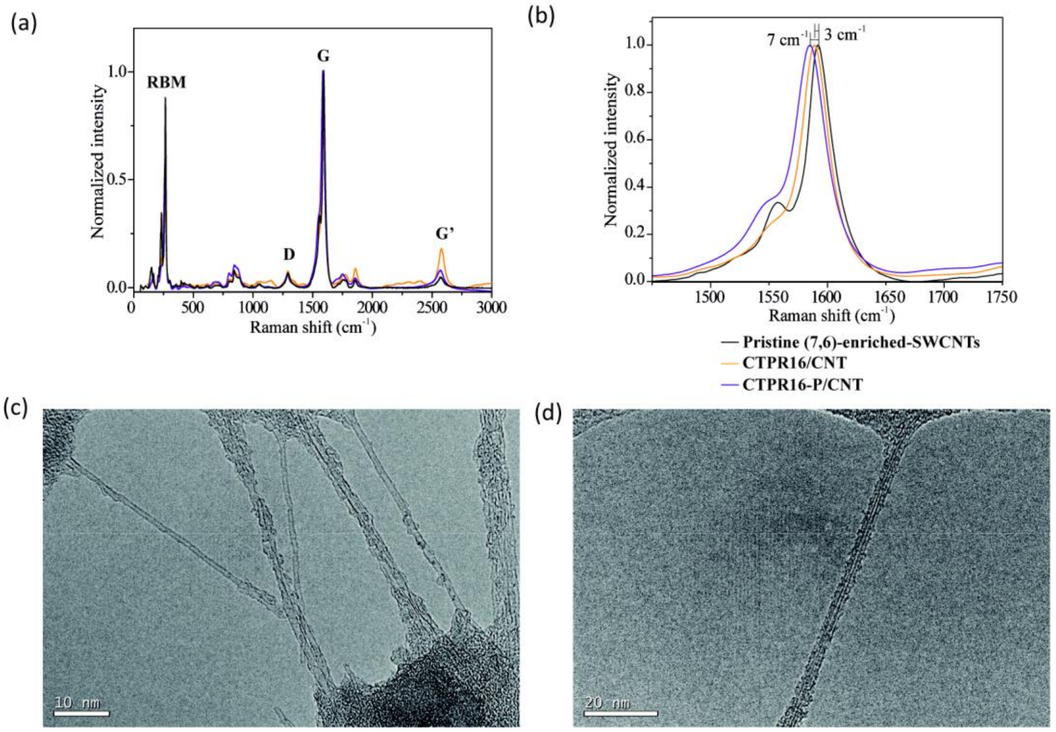

Figure 6. Raman spectroscopy and TEM images of the bio-organic nanohybrids. (a) Normalized Raman spectra from 50 to 3000 cm^{-1}. (b) Normalized Raman spectra in the region of G-mode. All of them have been acquired at an excitation wavelength of 785 nm. Pristine SWCNTs (black line), CTPR16/CNT (yellow line), CTPR16-P/CNT (purple line). (c) TEM image of CTPR16/CNT nanohybrids. (d) TEM image of CTPR16-P/CNT nanohybrids.

Transmission electron microscopy (TEM) provided conclusive support of the existence of the protein-CNT and conjugate-CNT nanohybrids. TEM images were acquired by drop-casting the corresponding aqueous solution onto a carbon grid. Figures 6c,d and S6 show that the nanotubes are in an excellent exfoliated state and most of the individual SWCNTs showed their walls covered by organic material, that is, the protein or the conjugate depending on the sample.

In our previous work, we described that these porphyrin-protein conjugates preserve their structural integrity in the solid state, when forming thin films.[5] Now, we produced the aforementioned thin films with these new hybrid materials and tested their features by X-ray diffraction (XRD). XRD data of the mutated CTPR16, its conjugate CTPR16-P and their corresponding nanohybrids CTPR16/CNT and CTPR16-P/CNT all revealed a most intense broad signal at 2θ around 19 to 21° (Figure S7). This value with a *d*-spacing of around 0.43 nm has been previously associated to the α-helical pitch of tandem repeats configuring the superhelix.[14] Therefore, CTPR16 scaffold retained its superhelical conformation both with the enormous amount of porphyrins covalently attached to the structure and, more challenging, the interacting SWCNTs.

2.4. **Charge carrier transporting properties of the bio-nanohybrids.**

The present soluble nanohybrids accommodating conducting SWCNT and photoactive porphyrin systems are interesting for soft electronics or bioelectronics fields. The photo-carrier injection and intrinsic charge carrier transporting properties were investigated by flash-photolysis microwave conductivity (FP-TRMC) technique that enables the device-less, non-contact evaluation of transient conductivity upon photo-generated charge carriers in CTPR16-P, CTPR16/CNT, and CTPR16-P/CNT with minimized damage of the scaffold structures.[15] Similarly to the previous demonstration for CTPR4-P[9], a thin film of CTPR16-P showed a clear conductivity transient upon photoexcitation with 355 nm laser pulse (Figure 7) with long-lived stable charge carrier species, suggesting significant contribution from the local motion of positive charge carriers on P-arrays. Transient absorption spectra support the formation of photo-oxidized states on the P-arrays (Figure S8), and the calculated yield of radical cations are □ = 4.0 × 10^{-2}, leading the local mobility of holes on P-arrays as □ = 4.5 × 10^{-3} cm^2 V^{-1} s^{-1}. A dropcast film of CTPR16/CNT provided a transient with prompt rise and moderate decay features. Namely, water-processable CTPR16/CNT films retain the conductivity of CNTs. We disclosed that CTPR16-P/CNT displayed a conductivity transient whose profile was almost identical to that of CTPR16/CNT, indicating that the major charge carriers of electrons were injected into CNTs and mobile along the 1D-structures. The photoconductivity transients within ~ 10 ms (Figure S9) obeys almost 2nd order recombination kinetics, suggesting local diffusion of electrons on CNT controls the recombination of positive/negative charge carriers. Presence of Zn porphyrin chromophores resulted in the effective charge carrier availability of excitation light over wide wavelength ranges. For example, photoexcitation of CTPR16-P/CNT by 420 nm laser pulses also exhibited photoconductive nature. This observation suggested that Zn porphyrins absorbed visible lights and mobile charge carriers were generated on CNTs. Thus, nanohybrids of CTPR16-P/CNT revealed its excellent conductivity, photoabsorption capability, as well as water-based film processability.

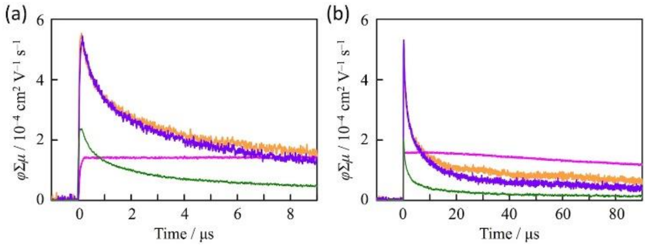

Figure 7. Kinetic traces of conductivity transients of a film of CTPR16-P (magenta), CTPR16/CNT (yellow), and CTPR16-P/CNT (purple) photoexcited at 355 nm, and CTPR16-P/CNT (green) photoexcited at 420 nm at the time range of (a) 10 µs and (b) 100 µs.

2. Conclusions.

In summary, we described a novel approach to achieve biomolecular electronic materials using a chemically modified protein as wrapping agent for SWCNTs. The optimal superhelical conformation of CTPR proteins and the possibility to mutate some residues to amino acids with potential larger interaction energies make them a good candidate to reach this goal. In this regard, we have demonstrated the effectiveness of our approach by a wide range of techniques, corroborating the introduction of the SWCNT into the inner cavity of the protein superhelix and the stability of the folding state of the protein even with the carbon nanostructure inside. Additionally, we have performed a comparative study considering the length of the protein, using CTPR4, CTPR8 and CTPR16, which reveals that the increase in the protein length improves the wrapping capability and thereby the binding affinity for SWCNT.

Moreover, this approach has been expanded to the conjugates with photo and electroactive metallophorphyrins to obtain unprecedented biomolecular electronic nanohybrids, namely donor-acceptor protein-P-SWCNT. The ability of the protein-porphyrin conjugates for wrapping around (7,6)-SWCNTs has been demonstrated to be virtually identical than their corresponding non-conjugated proteins. However, it is important to remark two important features in these nanohybrids: i) the increase in the binding affinity due to the favorable interaction of the porphyrin moieties with the surface of the SWCNTs and, ii) a remarkable higher value of photoconductivity for these donor/acceptor bio-nanohybrids. All together, this bioinspired methodology paves the way to the use of repeat proteins as highly efficient, robust and chemically versatile scaffolds to obtain highly ordered and unprecedented functional materials.

Supporting Information

Supporting Information is available from the Wiley Online Library or from the author.

Acknowledgements

This work has been supported by the European Commission IRG-246688 Bionanotools (ALC), the Spanish Ministry of Economy and Competitiveness (MINECO) BIO2012-34835 and BIO2016-77367-C2-1-R (ALC) and CTQ2014-520456-R (NM) and the European Research Council ERC-320441-Chirallcarbon (NM), and ERC-2014-CoG-648071-ProNANO (ALC). NM thanks to Community of Madrid Government (Photocarbon project. S2013/MIT-2841). CA thanks to the Ramón y Cajal granted and JL-A thanks to Spanish Ministry of Education for FPU granted. SHM thanks the Basque Government for financial support through a PhD fellowship. F.F. thanks the European Community for MSCA-IF-2014-EF-661160-MetAccembly grant. S.O. thanks the Spanish MINECO CTQ2014-59212-P, Ramón y Cajal contract (RYC-2014-16846), the European Community for CIG project (PCIG14-GA-2013-630978), and the funding from the European Research Council (ERC) under the European Union's Horizon 2020 research and innovation program (ERC-2015-StG-679001-NetMoDEzyme).

Received: ((will be filled in by the editorial staff))
Revised: ((will be filled in by the editorial staff))
Published online: ((will be filled in by the editorial staff))

References

[1] a) M. Calvaresi, F. Zerbetto, *Acc. Chem. Res.* **2013**, *46*, 2454-2463; b) S. F. Oliveira, G. Bisker, N. A. Bakh, S. L. Gibbs, M. P. Landry, M. S. Strano, *Carbon* **2015**, *95*, 767-799.

[2] a) M. Zheng, A. Jagota, M. S. Strano, A. P. Santos, P. Barone, S. G. Chou, B. A. Diner, M. S. Dresselhaus, R. S. Mclean, G. B. Onoa, G. G. Samsonidze, E. D. Semke, M. Usrey, D. J. Walls, *Science* **2003**, *302*, 1545-1548; b) M. J. Zheng, A.; Semke, E. D.; Diner, B. A.; McLean, R. S.; Lustig, S. R.; Richardson, R. E.; Tassi, N. G., *Nat. Mater.* **2003**, *2*, 338; c) X. M. Tu, S.; Jagota, A.; Zheng, M., *Nature* **2009**, *460*.

[3] a) M. J. Pender, L. A. Sowards, J. D. Hartgerink, M. O. Stone, R. R. Naik, *Nano. Lett.* **2006**, *6*, 40-44; b) S. Wang, E. S. Humphreys, S.-Y. Chung, D. F. Delduco, S. R. Lustig, H. Wang, K. N. Parker, N. W. Rizzo, S. Subramoney, Y.-M. Chiang, A. Jagota, *Nat. Mater.* **2003**, *2*, 196-200; c) Z. Li, T. Kameda, T. Isoshima, E. Kobatake, T. Tanaka, Y. Ito, M. Kawamoto, *Langmuir* **2015**, *31*, 3482-3488; d) G. Grigoryan, Y. H. Kim, R. Acharya, K. Axelrod, R. M. Jain, L. Willis, M. Drndic, J. M. Kikkawa, W. F. DeGrado, *Science* **2011**, *332*, 1071-1076; e) F. De Leo, A. Magistrato, D. Bonifazi, *Chem. Soc. Rev.* **2015**; fG. Zuo, Q. Huang, G. Wei, R. Zhou, H. Fang, *ACS Nano* **2010**, *4*, 7508-7514; g) J. S. F. De Leo, D. Bonifazi, A. Magistrato, *Chem. Eur. J.* **2013**, *19*, 12281-12294.

[4] F. D'Souza, S. K. Das, M. E. Zandler, A. S. Sandanayaka, O. Ito, *J. Am. Chem. Soc.* **2011**, *133*, 19922-19930.

[5] S. H. Mejías, J. López-Andarias, T. Sakurai, S. Yoneda, K. P. Erazo, S. Seki, C. Atienza, N. Martín, A. L. Cortajarena, *Chem. Sci.* **2016**, *7*, 4842-4847.

[6] a) L. D. D'Andrea, L. Regan, *Trends Biochem. Sci.* **2003**, *28*, 655-662; b) A. L. Cortajarena, S. G. J. Mochrie, L. Regan, *Protein Science* **2011**, *20*, 1042-1047.

[7] a) S. H. Mejias, A. Aires, P. Couleaud, A. L. Cortajarena, *Adv. Exp. Med. Biol.* **2016**, *940*, 61-81; b) D. Romera, P. Couleaud, S. H. Mejias, A. Aires, A. L. Cortajarena, *Biochem. Soc. Trans.* **2015**, *34*, 825-831.

[8] a) T. Kajander, A. L. Cortajarena, E. R. Main, S. G. Mochrie, L. Regan, *J. Am. Chem. Soc.* **2005**, *127*, 10188-10190; b) T. Kajander, A. L. Cortajarena, S. G. Mochrie, L. Regan, *Acta Crystallogr. D* **2007**, *D63*, 800-811.

[9] a) S. Az'hari, Y. Ghayeb, *Molecular Simulation* **2013**, *40*, 392-398; b) E. M. Perez, N. Martin, *Chem. Soc. Rev.* **2015**, *44*, 6425-6433.

[10] a) V. Z. Poenitzsch, D. C. Winters, H. Xie, G. R. Dieckmann, A. B. Dalton, I. H. Musselman, *J. Am. Chem. Soc.* **2007**, *129*, 14724-14732; b) S. Wang, E. S. Humphreys, S.-Y. Chung, D. F. Delduco, S. R. Lustig, H. Wang, K. N. Parker, N. W. Rizzo, S. Subramoney, Y.-M. Chiang, A. Jagota, *Nat. Mater.* **2003**, *2*, 196-200.

[11] A. L. Cortajarena, L. Regan, *Protein Sci.* **2006**, *15*, 1193-1198.

[12] Cohen SS, Riven I, Cortajarena AL, De Rosa L, D'Andrea LD, Regan L, H. G., *J. Am. Chem. Soc.* **2015**, *137*, 10367-10373.

[13] a) A. M. Rao, P. C. Eklund, S. Bandow, A. Thess, R. E. Smalley, *Nature* **1997**, *388*, 257-259; b) K. E. Wise, C. Park, E. J. Siochi, J. S. Harrison, *Chem. Phys. Lett.* **2004**, *391*, 207-211; c) R. Voggu, C. S. Rout, A. D. Franklin, T. S. Fisher, C. N. R. Rao, *J. Phys. Chem. C* **2008**, *112*, 13053-13056; d) F. G. Brunetti, C. Romero-Nieto, J. Lopez-Andarias, C. Atienza, J. L. Lopez, D. M. Guldi, N. Martin, *Angew. Chem.* **2013**, *52*, 2180-2184; e) C. Romero-Nieto, R. Garcia, M. A. Herranz, C. Ehli, M. Ruppert, A. Hirsch, D. M. Guldi, N. Martin, *J. Am. Chem. Soc.* **2012**, *134*, 9183-9192.

[14] T. Z. Grove, L. Regan, A. L. Cortajarena, *J. R. Soc. Interface.* **2013**, *10*, 20130051.

[15] S. Seki, A. Saeki, T. Sakurai, D. Sakamaki, *Phys. Chem. Chem. Phys.* **2014**, *16*, 11093-11113.

The table of contents entry should be 50–60 words long, and the first phrase should be bold. The entry should be written in the present tense and impersonal style. The text should be different from the abstract text.

Keyword Porphyrin, designed proteins, consensus tetratricopeptide repeat (CTPR), biomolecular templating, SWCNT, photoconductive materials

Javier López-Andarias,‡[a] *Sara H. Mejías,*‡[b] *Tsuneaki Sakurai,*[c] *Wakana Matsuda,*[c] *Shu Seki,*[c] *Ferran Feixas,*[d] *Sílvia Osuna,*[d] *Carmen Atienza,**[a] *Nazario Martín**[a],[b] *and Aitziber L. Cortajarena**[b],[e],[f]
* ((same order as byline))

Toward bioelectronic nanomaterials: photoconductivity in protein-porphyrin hybrids wrapped around SWCNT

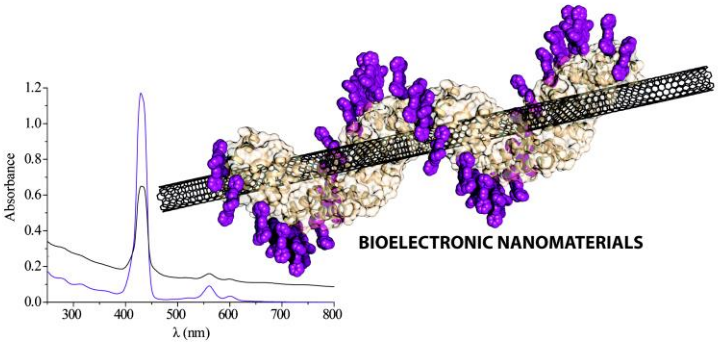

ToC figure ((Please choose one size: 55 mm broad × 50 mm high **or** 110 mm broad × 20 mm high. Please do not use any other dimensions))

((Supporting Information can be included here using this template))

Supporting Information

Toward bioelectronics materials: efficient photoconductivity in protein-porphyrin hybrids wrapped around SWCNT

Javier López-Andarias,‡[a] Sara H. Mejías,‡[b] Tsuneaki Sakurai,[c] Wakana Matsuda,[c] Shu Seki,[c] Ferran Feixas,[d] Silvia Osuna,[d] Carmen Atienza,*[a] Nazario Martín*[ab] and Aitziber L. Cortajarena*[b,e,f]

Contents:

C. Computational Methods

A. Materials, techniques and experimental procedure.

Protein design and purification. Based on a consensus CTPR protein, two cysteine residues were introduced in the CTPR repeat at positions 15 and 17 within the loop connecting the helix A and B within the repeat. The mutations were introduced in the gene encoding 1 repeat (CTPR1) by quickchange site directed mutagenesis. The **CTPR4**, **CTPR8** and **CTPR16** genes were generated from the CTPR1 mutated gene by sequential additions of identical mutated repeats: (4 for **CTPR4**, 8 for **CTPR8,** and 16 for **CTPR16**) and cloned into pPro-EXHTa vector. The protein was expressed as His-tagged fusion and purified using standard affinity chromatography methods based on previously published protocols for His-tagged CTPR proteins using 0.5% deoxycholic acid in the lysis buffer. The proteins were dialyzed into PBS buffer (150 mM NaCl, 50 mM phosphate buffer pH 7.4) and stored frozen at –20°C. The protein concentration was determined by UV-absorbance at 280nm using the extinction coefficient calculated from the amino acid composition of **CTPR4**, **CTPR8** and **CTPR16** (51800 M^{-1} cm^{-1}, 97640 M^{-1} cm^{-1} and 189320 M^{-1} cm^{-1} respectively).

Preparation of metalloporphyrin derivative P. The corresponding compound **P** was synthetized using a previously reported procedure described by our research group.

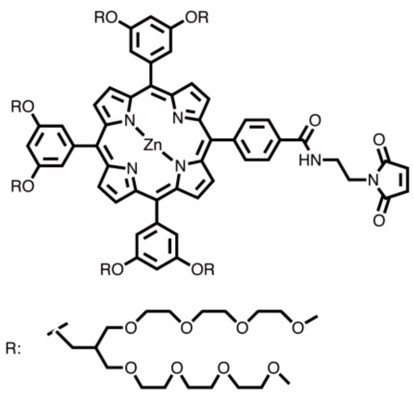

CTPR4/8/16-P conjugations. Prior to any conjugation, purified **CTPR4/8/16** at a protein concentration of about 100μM was freshly reduced with 1 mM 1,4-dithio-DL-treitol (DTT) during 20 minutes to ensure full reduction of the cysteine residues. DTT was removed by buffer exchange over a NAP-5 column (GE Healthcare Life Science) in PBS buffer. Protein fractions without DTT are collected at 4ºC and 1mM TCEP was added to avoid the formation of disulfide bonds between cysteines during the conjugation reaction. The protein concentration was measured by UV-absorbance. 300 µl of 50 µM, 25 µM or 12.5 µM of freshly reduced **CTPR4**, **CTPR8** or **CTPR16** protein, respectively, was mixed with 40 equivalents of **P** (around 1.9 mg) giving a ratio of 1:5 cysteine:maleimide and mixed gently. After an hour, an extra of 20 equivalents of **P** was added to the mixture (around 1 mg) giving a final ratio 1:7.5 cysteine:maleimide. The reaction mixture was incubated during 3 hours shaking and protected from light. 15% SDS-PAGE electrophoresis gels were used to monitor the conjugation process. Samples of the **CTPR4/8/16** protein controls and marker were prepared using Amresco EZ-vision loading buffer and the conjugates were mixed with SDS loading buffer. The gel prior staining was imaged using UV-light to monitor the fluorescence of the porphyrin **P**. Then, the gels were stained with Coomassie Blue.

Gel filtration chromatography. To purify the conjugates from the free porphyrin gel filtration chromatography was performed using an AKTA prime plus Fast Protein Liquid Chromatography (FPLC) equipment (GE Healthcare). The conjugation reaction was injected into a Superdex 75 HR 10/30 size exclusion chromatography column (GE Healthcare) and run at 0.5 mL/min in PBS buffer. The purified samples were collected in 0.5 mL fractions and stored protected from light.

Wrapping of SWCNTs with proteins and conjugates. Firstly, the absorbance at λ = 280 nm of the corresponding **CTPR4**, **CTPR8** and **CTPR16** mutated proteins was adjusted to 0.13, that is, a final concentration of 2.5 µM, 1.25 µM and 0.63 µM, respectively, in PBS buffer. These molar concentration implied a weight/volume percent of 0.005% (w/v) for all the samples. Meanwhile, in the case of **CTPR4-P**, **CTPR8-P** and **CTPR16-P** conjugates, the same strategy was followed, adjusting the absorbance at λ = 280 nm to 0.13.

Secondly, 2 mL of each sample were transferred to a glass vial and were sonicated in an ultrasound bath in the presence of around 1 mg of (7,6)-enriched SWCNTs. The temperature of the bath was maintained at around 15-20ºC to avoid denaturation of the proteins. Every 15 min, each dispersion was transferred to a microcentrifuge tube and was centrifuged at 12000 r.p.m. for 3 min. The 75% of the supernatant was recovered from the centrifugation tubes, avoiding sediment at the bottom, and was transferred to an absorbance cuvette for monitoring the amount of wrapped SWCNTs. This process was repeated until no more changes in the UV-vis spectra were observed.

Finally, the supernatant obtained for all nanohybrids was centrifuged 30 min more at 5000 r.p.m. to perfectly remove the non-functionalized SWCNTs, obtaining clear solutions in all the cases. These solutions were kept in the fridge where they remained stable over months.

In the case of the control experiment with non-conjugated **P**, to a solution containing **P** (6.1 µM in PBS buffer) around 1 mg of SWCNTs was added and the same aforementioned procedure was followed, that is, prolonged sonication and high-rating centrifugation.

Absorbance measurements. Absorbance spectra were recorded using a VARIAN-80 UV-*vis* spectrophotometer. The absorbance spectra of the protein, porphyrin, and protein-porphyrin conjugates from 230 nm to 1000 nm were acquired in a 1 cm pathlength quartz cuvette using a 4 nm slit-width.

Circular dichroism (CD) measurements. CD spectra were measured using a Jasco J-815 CD Spectrometer. CD spectra of proteins, conjugates and nanohybrids in water were acquired in a 1 mm path length quartz cuvette at a protein concentration of around 10 µM. All the CD spectra were recorded with a band-width of 1 nm at 1 nm increments and 4 second average time.

Transmission Electron Microscopy (TEM). TEM images were performed in a JEOL JEM 1011 electron microscope operated at 100 kV. Images were directly recorded using a GATAN Erlangshen ES 1000W camera attached to the microscope.

X-ray Diffraction (XRD). X-ray diffraction was performed in a Panalytical X'Pert PRO diffractometer with Cu tube (lambda Kα=1.54187 Å) operated at 45 kV, 40 mA, Ni beta filter, programmable divergence and anti-scatter slits working in fixed mode, and fast linear detector (X'Celerator) working in scanning mode.

Flash-photolysis time-resolved microwave conductivity (FP-TRMC). The charge carrier transport property along the π-stacked porphyrin assemblies was evaluated by FP-TRMC technique at room temperature under air. Uniform thin films were prepared on a quartz plate by dropcasting of deionized water solution of **CTPR16**, **CTPR16/CNT**, and **CTPR16-P/CNT**. Transient charge carriers were generated through photoexcitation by laser pulses of third harmonic generation (λ□= 355 nm) from a Spectra Physics model INDI-HG Nd:YAG laser with a pulse duration of 5–8 ns. Light pulses at 420 nm were also used as excitation light source from a Spectra Physics model versaScan optical parametric oscillator unit pumped with THG pulses of an identical laser system. The photon density of a 355 nm and 420 nm pulse was set at 4.6×10^{15} and 8.1×10^{15} photons cm^{-2} pulse^{-1}, respectively. The probing microwave frequency and power were set at 9.1 GHz and 3 mW, respectively. Photoconductivity transients, demodulated through a GaAs crystal-diode with Schottky-barriers (rise time < 1 ns), were monitored by a Tektronix model TDS3032B digital oscilloscope. The observed conductivities were normalized, given by a photocarrier generation yield (φ) multiplied by sum of the charge carrier mobilities ($\Sigma\mu$), according to the equation,

$$f \sum m = \frac{A \mathrm{D} P_{\mathrm{r}}}{e I_0 F_{\mathrm{L}} P_{\mathrm{r}}}$$

where, e, A, I_0, F_{light}, P_{r}, and ΔP_{r} are elementary charge, sensitivity factor (S cm^{-1}), incident photon density of the excitation laser (photon cm^{-2}), correction factor (cm^{-1}), and reflected microwave power and its change, respectively.

Transient absorption spectroscopy (TAS). Transient absorption spectroscopy (TAS) measurements were carried out at room temperature under air. The same dropcasted films used for FP-TRMC measurements were used for TAS measurements. The film was photoexcited using the third harmonic generation (λ = 355 nm) from the identical Spectra Physics laser, where the photon density of a 355 nm pulse was 4.6×10^{15} photons cm^{-2} pulse^{-1}. A white light continuum from a Xe lamp was used as a probe light source for transient absorption spectroscopy. The monochromated probe light was guided into a Hamamatsu model C7700 wide-dynamic-range streak camera system, which collected a two-dimensional image of the spectral and temporal profiles of light intensity.

B. Supplementary figures

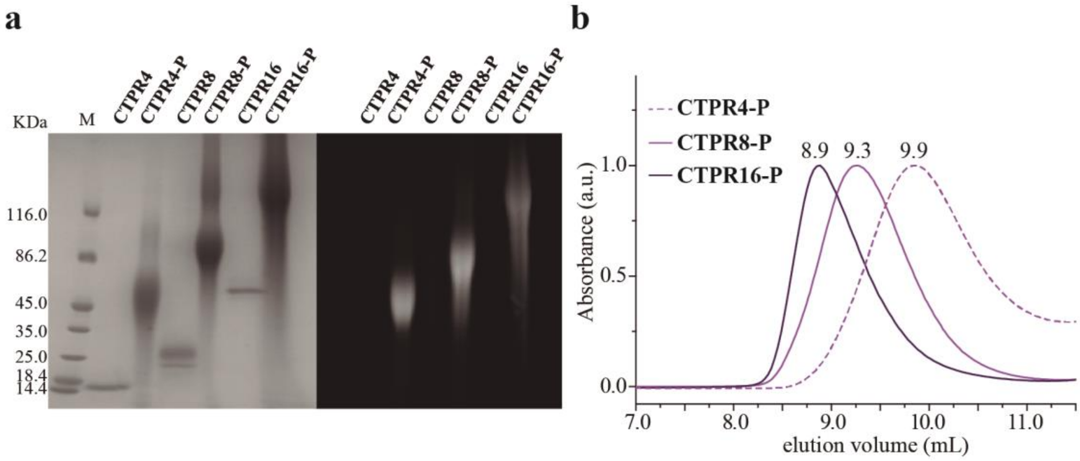

Figure S1. Analysis and purification of conjugates. (a) SDS-Page electrophoresis gel of the conjugation reactions: Molecular weight marker (lane 1), CTPR control proteins (lane 2, 4 and 6) and CTPR-porphyrin conjugates (lane 3, 5 and 7). The gel is shown prior staining imaged using UV-light to monitor the fluorescence of the porphyrins (right panel) and after Coomassie Blue staining (left panel). (b) Size exclusion chromatogram showing the different elution volumes of the three conjugates.

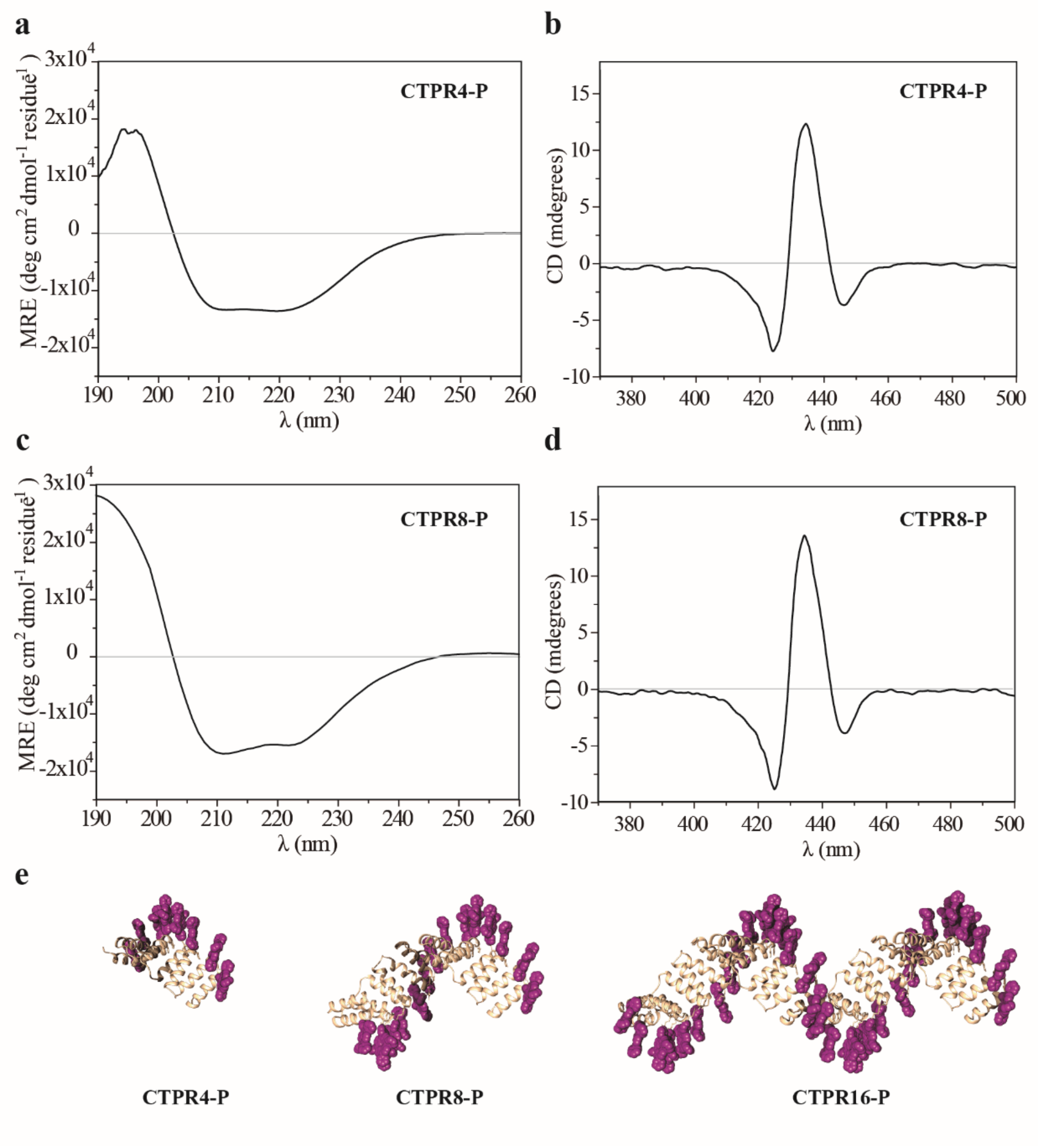

Figure S2. Spectroscopic characterization of bio-organic conjugates. (a) CD spectra of the **CTPR4-P** conjugate in the protein absorption region and (b) in the Soret band absorption region of the zinc-metalloporphyrin. (c) CD spectra of the **CTPR8-P** conjugate in the protein absorption region and (d) in the Soret band absorption region of the zinc-metalloporphyrin. (e) Representation of the three conjugates.

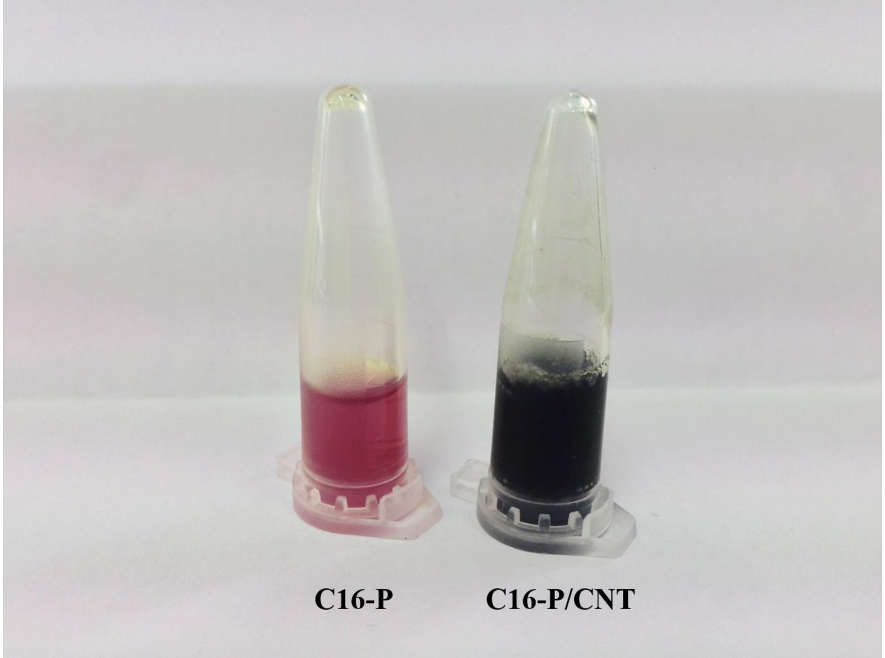

Figure S3. Photographs of a solution containing C16-P conjugate (left) and its corresponding C16-P/CNT nanohybrid (right).

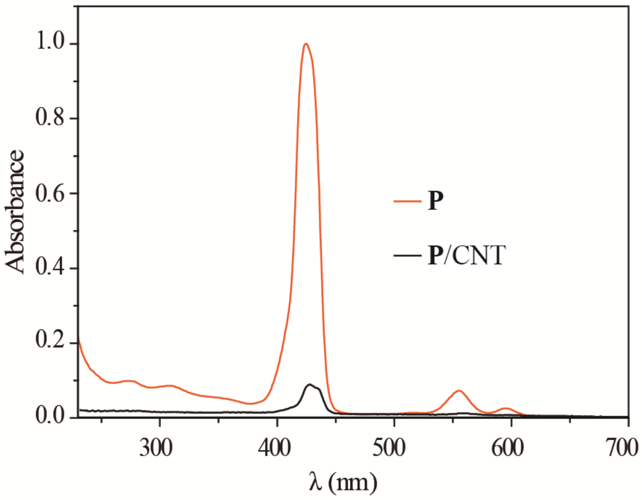

Figure S4. UV-*vis* spectra of P (orange line) and P/CNT (black line).

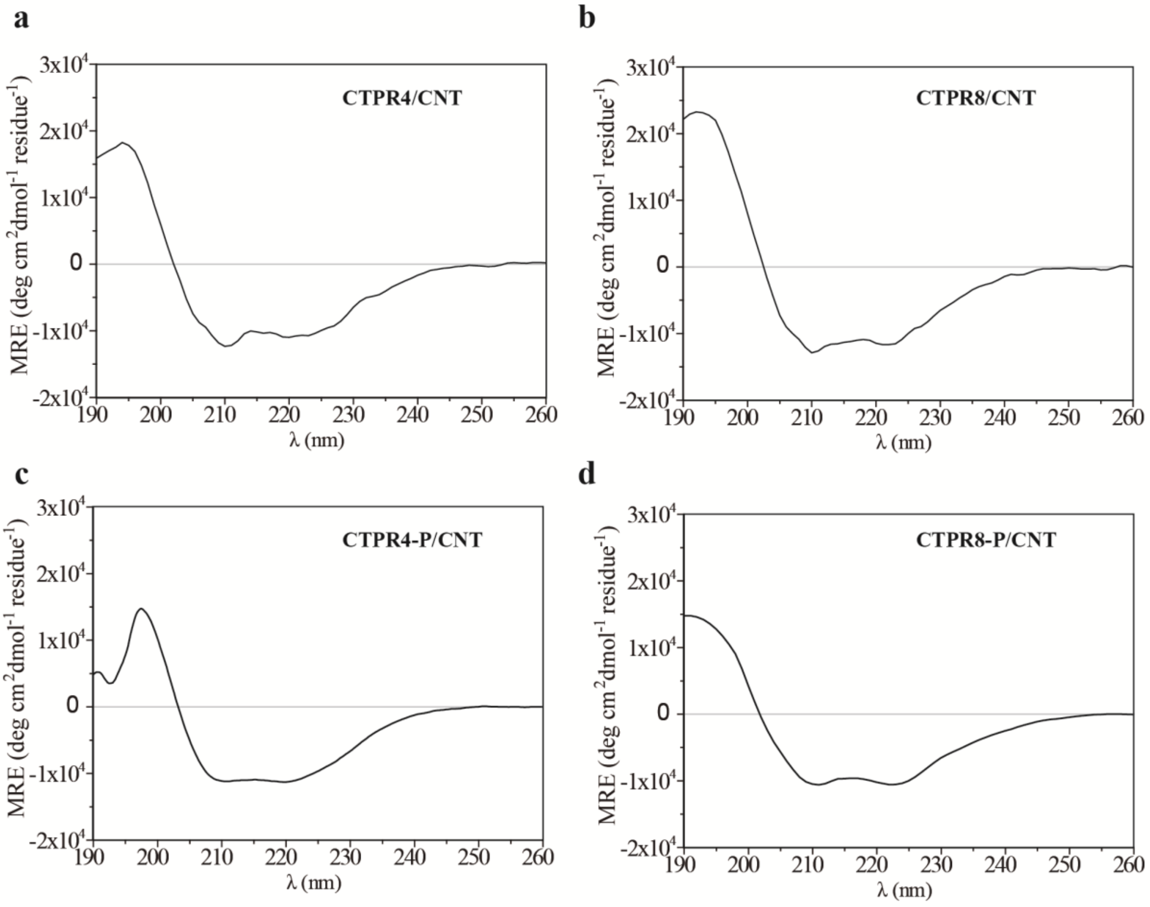

Figure S5. CD spectra of CTPR4 (a) and CTPR8 (b) proteins and their corresponding conjugates, CTPR4-P (c) and CTPR8-P (d) in the presence of SWCNTs.

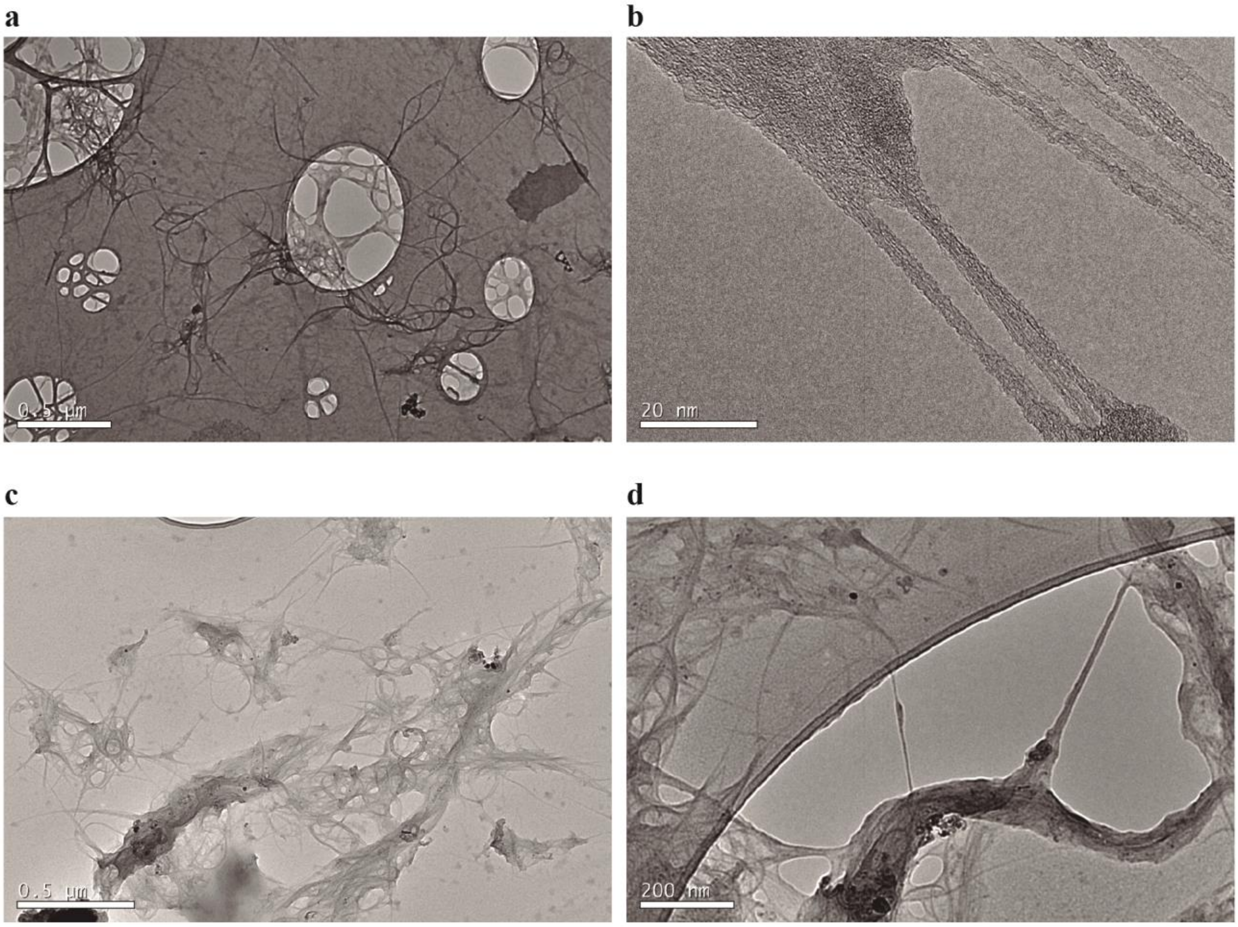

Figure S6. TEM micrographs at different magnifications. (a, b) CTPR16/SWCNT. (c,d) CTPR16-P/SWCNT.

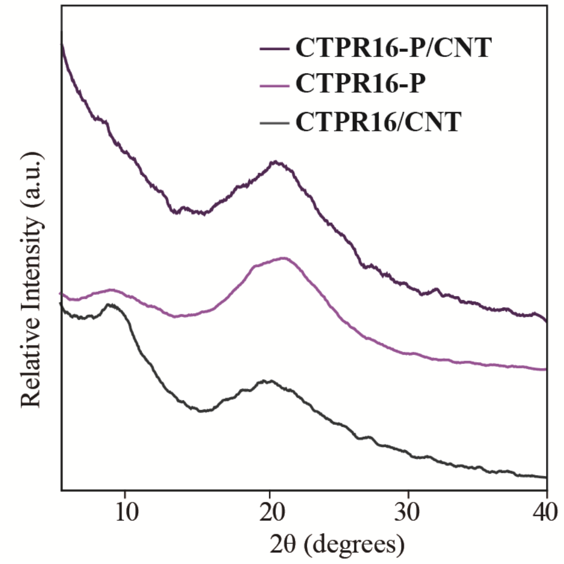

Figure S7. X-ray diffractograms of the films.

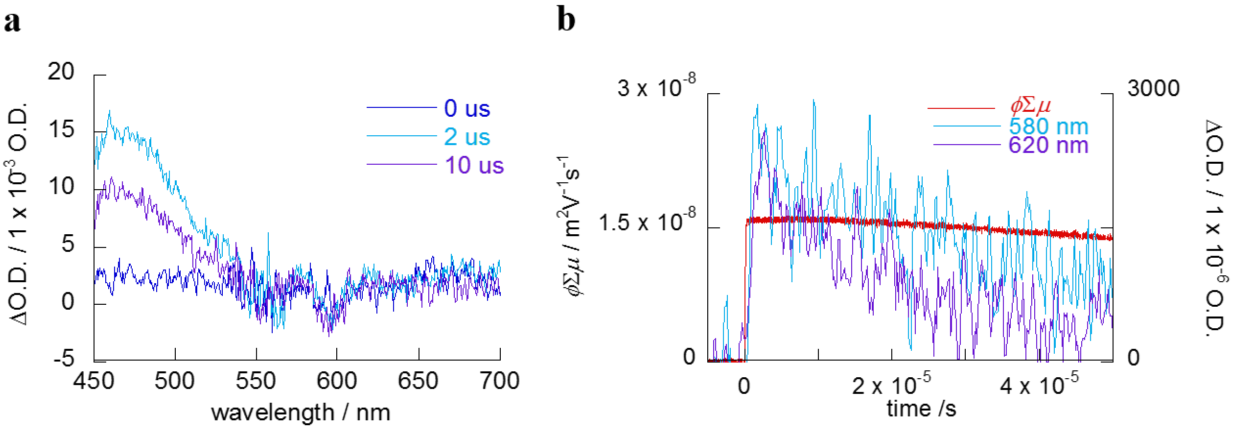

Figure S8. (a) Transient absorption spectra recorded for **CTPR16-P** upon photoexcitation at 355 nm, 4.6 × 10^{15} cm^{-2} $pulse^{-1}$, (b) kinetic traces observed at 580 and 620 nm with the photoconductivity trace.

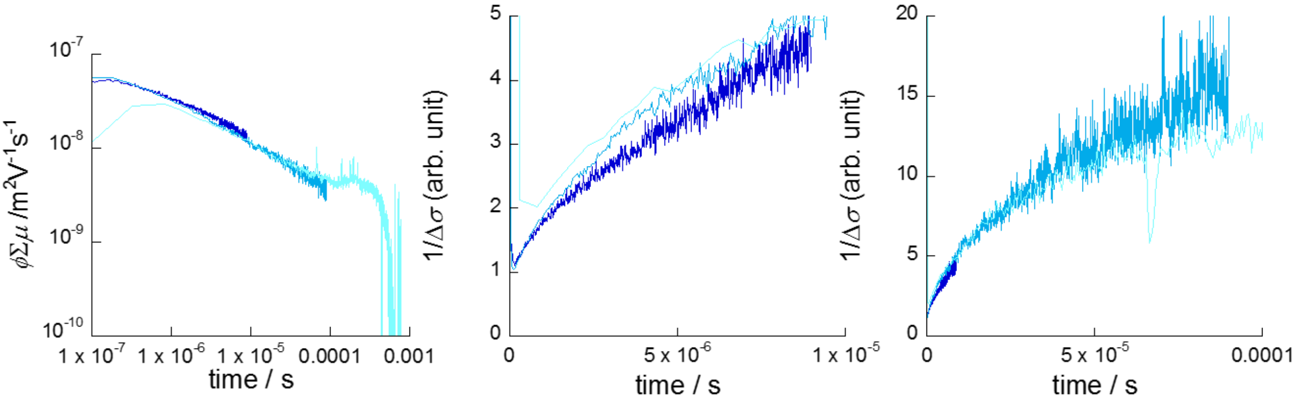

Figure S9. Photoconductivity kinetic traces recorded for **CTPR16-P/CNT** upon photoexcitation at 355 nm, 4.6 × 10^{15} cm^{-2} pulse^{-1}.

C. Computational Methods

Molecular Dynamics Simulations. Porphyrin parameters for the MD simulations were generated within the ANTECHAMBER module of AMBER 14 using the general AMBER force field (GAFF), with partial charges set to fit the electrostatic potential generated at the HF/6-31G(d) level by the RESP model. The charges were calculated according to the Merz-Singh-Kollman scheme using Gaussian 09. Each nanohybrid unit was immersed in a pre-equilibrated truncated octahedral box of water molecules with an internal offset distance of 12 Å, using the LEAP module. All systems were neutral, and no explicit counterions were added. A two-stage geometry optimization approach was performed. First, a short minimization of the water molecules positions, with positional restraints on solute by a harmonic potential with a force constant of 500 kcal mol^{-1} Å^{-2} was done. The second stage was an unrestrained minimization of all the atoms in the simulation cell. Then, the systems were gently heated using six 50 ps steps, incrementing the temperature 50 K each step (0-300 K) under constant-volume, periodic-boundary conditions and the particle-mesh Ewald approach to introduce long range electrostatic effects. For these steps, a 8 Å cutoff was applied to Lennard-Jones and electrostatic interactions. Bonds involving hydrogen were constrained with the SHAKE algorithm. Harmonic restraints of 10 kcal mol^{-1} were applied to the solute, and the Langevin equilibration scheme is used to control and equalize the temperature. The time step was kept at 1 fs during the heating stages, allowing potential inhomogeneities to self-adjust. Each system is then equilibrated for 2 ns with a 2 fs timestep at a constant pressure of 1 atm. Finally, a 100 ns unrestrained MD trajectory at constant volume and temperature (300 K) was collected, followed by 100 ns of dual-boost accelerated Molecular Dynamics (aMD). aMD enhances the conformational sampling of biomolecules, by adding a non-negative boost potential to the system when the system potential is lower than a reference energy:

$$V^*(r) = V(r), \qquad V(r) \geq E,$$

$$V^*(r) = V(r) + \Delta V(r),\quad V(r) < E, \qquad (1)$$

where $V(r)$ is the original potential, E is the reference energy, and $V^*(r)$ is the modified potential. In the simplest form, the boost potential, $\Delta V(r)$ is given by:

$$\Delta V(r) = \frac{(E - V(r))^2}{\alpha + E - V(r)}, \qquad (2)$$

where α is the acceleration factor. As the acceleration factor α decreases, the energy surface is flattened more and biomolecular transitions between the low-energy states are increased.

Here a total boost potential is applied to all atoms in the system in addition to a more aggressive dihedral boost, *i.e.*, (E_{dihed}, α_{dihed}; E_{total}, α_{total}), within the dual-boost aMD approach. The acceleration parameters used in this work, are the following:

$$E_{\mathrm{dihed}} = V_{\mathrm{dihed\_avg}} + 3.5 \times N_{\mathrm{res}},\ \alpha_{\mathrm{dihed}} = 3.5 \times N_{\mathrm{res}}/5;$$

$$E_{\mathrm{total}} = V_{\mathrm{total\_avg}} + 0.165 \times N_{\mathrm{atoms}},\ \alpha_{\mathrm{total}} = 0.165 \times N_{\mathrm{atoms}}, \qquad (3)$$

where N_{res} is the number of protein residues, N_{atoms} is the total number of atoms, and $V_{\mathrm{dihed\_avg}}$ and $V_{\mathrm{total\_avg}}$ are the average dihedral and total potential energies calculated from 100 ns MD simulations, respectively.

All trajectories were analyzed using the PTRAJ module in AMBER, and binding energies computed using MM-GBSA method as released in Ambertools12.

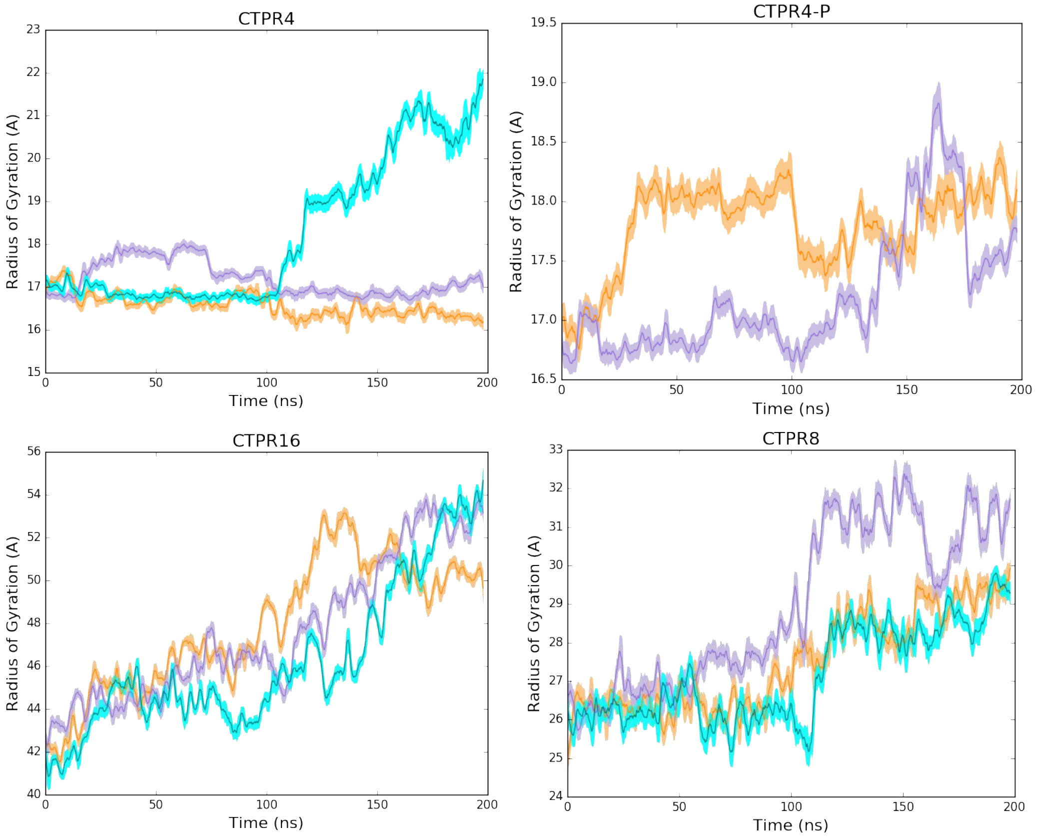

Figure S10. Representation of the Radius of Gyration (in Å) along the 3 replicas of 200 ns. MD simulations for **CTPR4**, **CTPR4-P**, **CTPR8**, **CTPR16** systems in the presence of a 20 nm long (7,6) SWCNT.

Table S1. Computed MM-GBSA Binding Energies (BE) together with the standard deviation (SD) (in kcal/mol) along the (a)MD simulations for the three replicas of the SWCNT-**CTPR4** systems. The average BE value is also provided (in kcal/mol).

		25ns		50ns		75ns		100ns		
	CTPR4	BE	SD	BE	SD	BE	SD	BE	SD	AVG
Replica1	MD	-140.58	10.29	-144.95	5.15	-141.02	5.05	-146.88	4.95	-143.36
	aMD	-177.28	27.59	-238.54	11.68	-277.93	14.25	-298.81	16.33	-248.14
Replica2	MD	-122.36	16.05	-137.54	6.36	-143.90	7.55	-148.34	6.07	-138.03
	aMD	-150.62	6.94	-162.48	8.57	-160.36	8.56	-154.53	8.12	-157.00
Replica3	MD	-109.47	8.69	-139.59	13.39	-149.18	6.86	-147.74	7.39	-136.49
	aMD	-105.62	63.61	-145.06	8.84	-150.31	7.77	-155.31	8.21	-139.07

Table S2. Computed MM-GBSA Binding Energies (BE) together with the standard deviation (SD) (in kcal/mol) along the (a) MD simulations for the three replicas of the SWCNT-**CTPR8** systems. The average BE value is also provided (in kcal/mol).

		25ns		50ns		75ns		100ns		
	CTPR8	BE	SD	BE	SD	BE	SD	BE	SD	AVG
Replica1	MD	-242.66	8.76	-236.30	7.38	-255.55	14.64	-282.11	6.34	-254.16
	aMD	-293.77	10.89	-296.85	14.51	-339.94	16.08	-329.53	54.58	-315.02
Replica2	MD	-199.87	7.25	-202.28	7.39	-202.56	7.61	-211.87	15.29	-204.14
	aMD	-161.40	71.20	-167.70	59.20	-199.88	85.62	-312.65	10.53	-210.41
Replica3	MD	-232.06	6.73	-230.59	5.93	-234.03	6.79	-233.49	6.53	-232.54
	aMD	-251.94	15.22	-266.79	57.62	-321.41	30.53	-323.14	12.02	-290.82

Table S3. Computed MM-GBSA Binding Energies (BE) together with the standard deviation (SD) (in kcal/mol) along the (a) MD simulations for the three replicas of the SWCNT-**CTPR16** systems. The average BE value is also provided (in kcal/mol).

		25ns		50ns		75ns		100ns		
	CTPR16	BE	SD	BE	SD	BE	SD	BE	SD	AVG
Replica1	MD	-407.5	12.5	-432.5	9.3	-445.3	15.3	-452.9	12.3	-434.6
	aMD	-511.5	31.1	-600.1	13.4	-633.3	16.4	-644.3	12.3	-597.3
Replica2	MD	-428.2	13.7	-438.3	11.2	-428.9	11.7	-418.6	50.8	-428.5
	aMD	-458.3	43.7	-542.4	64.1	-610.5	70.4	-572.4	45.1	-545.9
Replica3	MD	-452.1	11.6	-444.6	11.1	-455.5	10.5	-449.4	9.8	-450.4
	aMD	-522.3	22.0	-538.3	14.8	-578.5	26.2	-645.4	23.4	-571.1

Table S4. Computed MM-GBSA Binding Energies (BE) together with the standard deviation (SD) (in kcal/mol) along the (a) MD simulations for the three replicas of the SWCNT-**CTPR4-P** systems. The average BE value is also provided (in kcal/mol).

		25ns		50ns		75ns		100ns		
	CTPR4-P	BE	SD	BE	SD	BE	SD	BE	SD	AVG
Replica1	MD	-398.53	44.85	-446.34	14.66	-460.30	12.24	-463.38	14.45	-442.14
	aMD	-511.59	19.60	-552.11	20.76	-587.22	19.27	-600.61	14.92	-562.88
Replica2	MD	-341.11	58.91	-440.46	29.09	-463.13	11.96	-466.42	10.89	-427.78
	aMD	-468.68	15.07	-473.39	13.08	-473.41	12.12	-468.86	11.88	-471.09

References

(1) Kajander, T.; Cortajarena, A. L.; Regan, L. *Methods Mol. Biol.* **2006**, *340*, 151.

(2) Mejías, S. H.; López-Andarias, J.; Sakurai, T.; Yoneda, S.; Erazo, K. P.; Seki, Sh.; Atienza, C.; Martín, N.; Cortajarena, A. L. *Chem. Sci.* **2016**, *7*, 4842-4847

(2) Case, D. A.; Darden, T. A.; Cheatham, T. E.; Simmerling, C. L.; Wang, J.; Duke, R. E.; Luo, R.; Crowley, M.; Walker, R. C.; Zhang, W.; Merz, K. M.; Wang, B.; Hayik, S.; Roitberg, A.; Seabra, G.; Kolossváry, I.; Wong, K. F.; Paesani, F.; Vanicek, J.; Wu, X.; Brozell, S. R.; Steinbrecher, T.; Gohlke, H.; Yang, L.; Tan, C.; Mongan, J.; Hornak, V.; Cui, G.; Mathews, D. H.; Seetin, M. G.; Sagui, C.; Babin, V.; Kollman, P. A. *AMBER 12, University of California, San Francisco, 2012*.

(3) Wang, J.; Wolf, R. M.; Caldwell, J. W.; Kollman, P. A.; Case, D. A. *Journal of Computational Chemistry* **2004**, *25*, 1157.

(4) Bayly, C. I.; Cieplak, P.; Cornell, W.; Kollman, P. A. *The Journal of Physical Chemistry* **1993**, *97*, 10269.

(5) Besler, B. H.; Merz, K. M.; Kollman, P. A. *Journal of Computational Chemistry* **1990**, *11*, 431.

(6) Singh, U. C.; Kollman, P. A. *Journal of Computational Chemistry* **1984**, *5*, 129.

(7) Frisch, M. J.; Trucks, G. W.; Schlegel, H. B.; Scuseria, G. E.; Robb, M. A.; Cheeseman, J. R.; Scalmani, G.; Barone, V.; Mennucci, B.; Petersson, G. A.; Nakatsuji, H.; Caricato, M.; Li, X.; Hratchian, H. P.; Izmaylov, A. F.; Bloino, J.; Zheng, G.; Sonnenberg, J. L.; Hada, M.; Ehara, M.; Toyota, K.; Fukuda, R.; Hasegawa, J.; Ishida, M.; Nakajima, T.; Honda, Y.; Kitao, O.; Nakai, H.; Vreven, T.; Montgomery Jr., J. A.; Peralta, J. E.; Ogliaro, F.; Bearpark, M.; Heyd, J. J.; Brothers, E.; Kudin, K. N.; Staroverov, V. N.; Kobayashi, R.; Normand, J.; Raghavachari, K.; Rendell, A.; Burant, J. C.; Iyengar, S. S.; Tomasi, J.; Cossi, M.; Rega, N.; Millam, J. M.; Klene, M.; Knox, J. E.; Cross, J. B.; Bakken, V.; Adamo, C.;

Jaramillo, J.; Gomperts, R.; Stratmann, R. E.; Yazyev, O.; Austin, A. J.; Cammi, R.; Pomelli, C.; Ochterski, J. W.; Martin, R. L.; Morokuma, K.; Zakrzewski, V. G.; Voth, G. A.; Salvador, P.; Dannenberg, J. J.; S. Dapprich; Daniels, A. D.; Farkas, Ö.; Foresman, J. B.; Ortiz, J. V.; Cioslowski, J.; Fox, D. J.; Gaussian 09, Revision A.02 ed.; Gaussian, Inc.: Pittsburgh, PA, 2009.

(8) Schafmeister, C. E. A. F. R., W. F.; Romanovsky, V. University of California, San Francisco, 1995.

(9) Sagui, C.; Darden, T. A. *Annu. Rev. Biophys. Biomolec. Struct.* **1999**, *28*, 155.

(10) Ryckaert, J.-P.; Ciccotti, G.; Berendsen, H. J. C. *Journal of Computational Physics* **1977**, *23*, 327.

(11) Wu, X.; Brooks, B. R. *Chemical Physics Letters* **2003**, *381*, 512.

(12) Hamelberg, D.; Mongan, J.; McCammon, J. A. *The Journal of Chemical Physics* **2004**, *120*, 11919.

(13) Hamelberg, D.; Oliveira, C. A. F. d.; McCammon, J. A. *The Journal of Chemical Physics* **2007**, *127*, 155102.

((Please insert your Supporting Information text/figures here. Please note: Supporting Display items, should be referred to as Figure S1, Equation S2, etc., in the main text…)